Smart Structures and Systems, *Vol. 13, No. 4 (2014) 659-683*
DOI: http://dx.doi.org/10.12989/sss.2014.13.4.659

Nonhomogeneous atherosclerotic plaque analysis via enhanced 1D structural models

Alberto Varello[*1] and Erasmo Carrera[1,2a]

[1]*Department of Mechanical and Aerospace Engineering, Politecnico di Torino, Corso Duca degli Abruzzi 24, 10129 Torino, Italy*
[2]*Faculty of Science, King Abdulaziz University, Jeddah 21589, Saudi Arabia*

(Received May 11, 2013, Revised November 15, 2013, Accepted December 14, 2013)

Abstract. The static analysis of structures with arbitrary cross-section geometry and material lamination via a refined one-dimensional (1D) approach is presented in this paper. Higher-order 1D models with a variable order of expansion for the displacement field are developed on the basis of Carrera Unified Formulation (CUF). Classical Euler-Bernoulli and Timoshenko beam theories are obtained as particular cases of the first-order model. Numerical results of displacement, strain and stress are provided by using the finite element method (FEM) along the longitudinal direction for different configurations in excellent agreement with three-dimensional (3D) finite element solutions. In particular, a layered thin-walled cylinder is considered as first assessment with a laminated conventional cross-section. An atherosclerotic plaque is introduced as a typical structure with arbitrary cross-section geometry and studied for both the homogeneous and nonhomogeneous material cases through the 1D variable kinematic models. The analyses highlight limitations of classical beam theories and the importance of higher-order terms in accurately detecting in-plane cross-section deformation without introducing additional numerical problems. Comparisons with 3D finite element solutions prove that 1D CUF provides remarkable three-dimensional accuracy in the analysis of even short and nonhomogeneous structures with arbitrary geometry through a significant reduction in computational cost.

Keywords: refined 1D finite elements; unified formulation; higher-order models; arbitrary cross-section; nonhomogeneous material

1. Introduction

Recent numerical modeling advances in structural mechanics have provided in last decades key information on the biomechanics of arteries, from prediction of atherosclerotic plaque vulnerability (Cheng *et al*. 1993, Li *et al*. 2006) and aneurismal rupture (Rodríguez *et al*. 2008) to the effectiveness of stents (Capelli *et al*. 2009). In particular, a vulnerable plaque can be described as a large, soft lipid pool covered by a thin fibrous cap (Davies 1996). It is the rupture of this vulnerable plaque that ultimately leads to a break of the endothelium and the fibrous cap, exposure of the lipid pool and subsequent thrombosis and ischaemic sequelae (Li *et al*. 2006).

∗Corresponding author, Research assistant, Ph.D., E-mail: alberto.varello@polito.it
[a] Professor, E-mail: erasmo.carrera@polito.it, Website: www.mul2.com

http://www.techno-press.org/?journal=sss&subpage=8 ISSN: 1738-1584 (Print), 1738-1991 (Online)

Atherosclerotic cardiovascular disease is one of the leading causes of death in western countries (Petersen *et al*. 2005). As a consequence, an accurate understanding of the mechanical behavior of plaques under various loading conditions is an essential contributor for developing more insight in the physiology and pathophysiology of the cardiovascular system and new procedures for preventing or reducing restenosis (Holzapfel *et al*. 2004).

The advent of noninvasive high resolution imaging techniques such as intravascular ultrasound (IVUS) and magnetic resonance imaging (MRI) allows nowadays detailed morphological and structural characterization of arterial plaques to be performed in vivo (Yuan *et al*. 2002). Various experiments were also carried out to identify the material behavior of tissues constituting arterial plaques within the physiological loading domain (Holzapfel *et al*. 2004).

Several structural analyses of arterial plaques have been developed by many researchers from two-dimensional (2D) to three-dimensional (3D) models by means of the finite element method (FEM). 2D studies have shown that arterial wall geometry is a crucial factor influencing stress in the arterial wall and that stress in turn influences plaque rupture (Cheng *et al*. 1993, Li *et al*. 2006, Loree *et al*. 1992). Huang *et al*. (2001) used histology-based two-dimensional models for arterial plaque and found that thin fibrous caps with large lipid pools are important determinants of increased plaque stress. Gao and Long (2008) developed a single patient-based model from histological sections and by varying the size and structure of an atherosclerotic lesion they investigated its effect on the stress distribution within the wall by using 10-node 3D tetra elements. Li *et al*. (2008) created 2D cross-sectional models, investigating maximum stress locations and magnitudes. Kock *et al*. (2008) created a 2D finite element fluid-structure interaction model to investigate axial stresses at the plaque cap. Tang *et al*. (2008) constructed a 2D/3D patient specific multi-component model from in vivo MRI. Most recently, Gao *et al*. (2008) further expanded the use of in vivo MRI to investigate the stress distributions within four arteries and also considered the reliability of manual segmentation from MRI (Gao *et al*. 2009) using 10-node 3D tetra elements.

Typically, two-dimensional (2D) plate and shell or three-dimensional (3D) solid models are used to accurately model plaques and other biomechanical structures. Nonetheless, these approaches often reveal the disadvantage of a large number of degrees of freedom and hence a high computational cost. One main advantage of using instead one-dimensional (1D) models would be a reduced number of degrees of freedom (DOFs) and hence a lower computational cost compared with plate, shell and solid models (Bathe 1996). The 1D models used in early studies of slender structures were based on classical theories. Euler-Bernoulli theory (Euler 1744) neglected the transverse shear deformation completely. The first shear deformation theory of Timoshenko (Timoshenko 1921) assumed a constant shear strain across the cross-section. The growing use of advanced composite and sandwich materials in engineering has recently revealed that 1D theories have to be refined in order to predict the behavior of complex structures in an accurate way. However, the importance of refined 1D models is even more relevant in biomechanics in order to cope with arbitrary geometries and materials.

Over the last century an extensive work was done to introduce one-dimensional models for the analysis of thin-walled slender structures instead of two-dimensional and three-dimensional formulations (Kapania and Raciti 1989). A higher-order FE model based on classical laminated theory presented higher-frequencies analysis capabilities for the vibration response of laminated tapered beams (Ganesan and Zabihollah 2007a, b). Kant and Gupta (1988) proposed a refined FE higher-order model with quadratic transverse shear strain that was applied to the free vibration analysis of angle-ply laminated, deep sandwich and composite beams (Marur and Kant 1996,

2007). Tong *et al*. (1995) offered an analytical solution for free and forced vibrations of stepped generally non-uniform Timoshenko beams. A higher-order shear deformation theory was used by Ramalingerswara Rao and Ganesan (1995) to evaluate the harmonic response of tapered composite wings. Marur and Kant (1996) extended their work to the transient dynamic analysis of symmetric and unsymmetric sandwich and composite structures (Marur and Kant 1997). Na and Librescu (2001) studied nonuniform anisotropic thin-walled beams incorporating adaptive capabilities through a beam model with transverse shear and warping inhibition which was formulated by Librescu and Na (1998). As a particular case of dynamic response, the third-order shear deformation theory used by Şimşek (2010) indicated the importance of higher-order terms in correctly predicting the dynamic behavior of functionally graded (FG) beams and thus in tailoring FG material properties.

Recently, refined 1D theories such as those based on the 1D Carrera Unified Formulation (CUF) (Carrera *et al*. 2011) and variational asymptotic approach (VABS) (Yu *et al*. 2002) as well as the Generalized Beam Theory (GBT) (Silvestre and Camotim 2002) have presented remarkable advances in static, buckling, and free vibration analysis. In particular, CUF is a hierarchical formulation useful to obtain structural models of arbitrary order, including classical theories, by exploiting a systematic procedure. This formulation has been recently developed for the analysis of structures made of isotropic (Carrera *et al*. 2011, Carrera and Giunta 2010) and composite materials (Carrera and Petrolo 2012) via one-dimensional models. The advantages of using one-dimensional CUF models for the static, free vibration and forced dynamic analysis of beams with conventional cross-section geometries (square, rectangular, annular, etc.) were highlighted by Carrera and Giunta (2010), Carrera *et al*. (2012), and Carrera and Varello (2012).

The case studied in this paper is the structural analysis of a clinic artery case retrieved from the biomechanical literature (Holzapfel *et al*. 2004, Balzani *et al*. 2012). This example represents a preliminary application of the 1D CUF model to the study of a biomechanical case with arbitrary cross-section and nonhomogeneous materials. In the work of Balzani *et al*. (2012) only a two-dimensional structural simulation of the cross-section under a time-dependent internal blood pressure is carried out in order to keep the computational effort relatively low. This simplified approach totally neglects the important effects due to the third out-of-plane dimension. In general, these effects are fundamental especially in a biomechanical case where the haematic flow field and the non-standard structural behavior of biological tissues need a complete three-dimensional description. Obviously, the introduction of the third direction would typically need the use of solid (3D) elements instead of 2D plate or shell FEs and, consequently, a much higher computational effort. In order to take into account the out-of-plane direction and analyze a complete solid structure, 1D CUF models are thus here proposed since they require a low computational cost though showing remarkable three-dimensional performance.

2. Preliminaries

A structure with longitudinal axial length L and cross-section is typically considered and studied as a beam. A cartesian coordinate system is defined with axes x and z parallel to the cross-section, whereas y represents the longitudinal coordinate. The choice of the cross-section geometry is arbitrary as well as the material lamination, since they do not affect the following theoretical formulation. When the lamination of the material over the cross-section is nonhomogeneous, the cross-section can be subdivided into different subsections with their own

different laminations and arbitrary shapes. The sample case of three subsections is depicted in Fig. 1. The number of subsections is referred as N_S and the index k is employed to refer to the k^{th} subsection Ω_k. The cartesian components of the displacement vector $\boldsymbol{u}(x,y,z)$ are u_x, u_y, and u_z. The stress $\boldsymbol{\sigma}$ and the strain $\boldsymbol{\epsilon}$ components are grouped in vectors as follows

$$\begin{aligned} \boldsymbol{\sigma}_p &= \{\sigma_{zz} \quad \sigma_{xx} \ \sigma_{zx} \ \}^T & \boldsymbol{\varepsilon}_p &= \{\varepsilon_{zz} \quad \varepsilon_{xx} \ \varepsilon_{zx} \ \}^T \\ \boldsymbol{\sigma}_n &= \{\sigma_{zy} \quad \sigma_{xy} \ \sigma_{yy} \ \}^T & \boldsymbol{\varepsilon}_n &= \{\varepsilon_{zy} \quad \varepsilon_{xy} \ \varepsilon_{yy} \ \}^T \end{aligned} \tag{1}$$

where superscript T stands for the transposition operator. Subscripts p and n refer to quantities related to the beam cross-section and related to the out-of-plane direction, respectively. In the case of small displacements with respect to the length L, the linear relations between strain and displacement components hold and a compact vectorial notation can be adopted:

$$\begin{aligned} \boldsymbol{\varepsilon}_p &= \boldsymbol{D}_p \, \boldsymbol{u} \\ \boldsymbol{\varepsilon}_n &= \boldsymbol{D}_n \, \boldsymbol{u} = \boldsymbol{D}_{np} \, \boldsymbol{u} + \boldsymbol{D}_{ny} \, \boldsymbol{u} \end{aligned} \tag{2}$$

where $\boldsymbol{D}_p, \boldsymbol{D}_n, \boldsymbol{D}_{np}$, and $\boldsymbol{D}_{ny}$ are differential matrix operators defined in the work of Carrera and Varello (2012). The generalized Hooke's law for the k^{th} subsection of the nonhomogeneous cross-section is hence:

$$\begin{aligned} \boldsymbol{\sigma}_p^k &= \boldsymbol{C}_{pp}^k \boldsymbol{\varepsilon}_p + \boldsymbol{C}_{pn}^k \boldsymbol{\varepsilon}_n \\ \boldsymbol{\sigma}_n^k &= \boldsymbol{C}_{np}^k \boldsymbol{\varepsilon}_p + \boldsymbol{C}_{nn}^k \boldsymbol{\varepsilon}_n \end{aligned} \tag{3}$$

where $\boldsymbol{C}_{pp}^k$, $\boldsymbol{C}_{pn}^k$, $\boldsymbol{C}_{np}^k$, and $\boldsymbol{C}_{nn}^k$ are the matrices for the isotropic material which the k^{th} subsection is made of:

$$\boldsymbol{C}_{pp}^k = \begin{bmatrix} C_{11}^k & C_{12}^k & 0 \\ C_{12}^k & C_{22}^k & 0 \\ 0 & 0 & C_{44}^k \end{bmatrix}, \quad \boldsymbol{C}_{pn}^k = \boldsymbol{C}_{np}^{k\,T} = \begin{bmatrix} 0 & 0 & C_{13}^k \\ 0 & 0 & C_{23}^k \\ 0 & 0 & 0 \end{bmatrix}, \quad \boldsymbol{C}_{nn}^k = \begin{bmatrix} C_{55}^k & 0 & 0 \\ 0 & C_{66}^k & 0 \\ 0 & 0 & C_{33}^k \end{bmatrix} \tag{4}$$

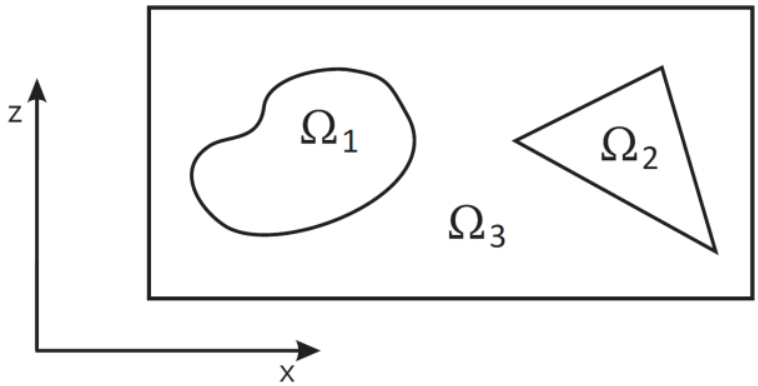

Fig. 1 Example of an arbitrary nonhomogeneous cross-section with three subsections ($N_S = 3$)

Through this approach, also the study of homogeneous structures (no subsections) is trivial and more details can be found in the work of Carrera and Varello (2012). For the sake of brevity, the dependence of the coefficients C_{ij}^{k} on Young's modulus, Poisson's ratio, and shear modulus is not reported here, but can be found in Jones (1999). In this paper isotropic materials for the nonhomogeneous structure are considered, but an extension of the following theoretical framework to orthotropic materials in analyzing laminated structures can be found in Carrera and Petrolo (2012).

3. Variable kinematic 1D models

According to the framework of Carrera Unified Formulation (CUF) (Carrera *et al*. 2011), the displacement field is assumed to be an expansion of a certain class of functions F_τ, which depend on the cross-section coordinates x and z:

$$\boldsymbol{u}(x,y,z) = F_\tau(x,z)\boldsymbol{u}_\tau(y) \qquad \tau = 1,2,\dots,N_u = (N+1)(N+2)/2 \tag{5}$$

The compact expression is based on Einstein's notation: repeated subscript τ indicates summation. Eq. (5) represents the general formulation of a one-dimensional (1D) theory, where the three-dimensional displacement field is axiomatically expressed in terms of general unknowns $\boldsymbol{u}_\tau$ depending on the longitudinal coordinate y. Multivariate Taylor's polynomials of the x and z variables are employed here as cross-section functions F_τ and N is defined as the expansion order, which is a free parameter of the formulation. Most displacement-based 1D theories can be formulated on the basis of the generic kinematic field in Eq. (5). For instance, when $N = 2$, the second-order axiomatic displacement field is given by:

$$\begin{aligned} u_x &= u_{x1} + u_{x2}\,x + u_{x3}\,z + u_{x4}\,x^2 + u_{x5}\,xz + u_{x6}\,z^2 \\ u_y &= u_{y1} + u_{y2}\,x + u_{y3}\,z + u_{y4}\,x^2 + u_{y5}\,xz + u_{y6}\,z^2 \\ u_z &= u_{z1} + u_{z2}\,x + u_{z3}\,z + u_{z4}\,x^2 + u_{z5}\,xz + u_{z6}\,z^2 \end{aligned} \tag{6}$$

Classical beam models such as Euler-Bernoulli's (EBBM) (Euler 1744) and Timoshenko's (TBM) (Timoshenko 1921) are easily derived from the first-order approximation model. Timoshenko beam model (TBM) can be obtained by setting terms $\{u_{ij} : i = x,z;\ j = 2,3\}$ equal to zero. An infinite rigidity in the transverse shear is also adopted for EBBM by penalizing ε_{yz} and ε_{xy} via a high penalty value (Carrera and Varello 2012) on each of the N_S subsection material coefficients C_{55}^{k} and C_{66}^{k}, $\{k = 1,\dots,N_S\}$. Higher-order models provide an accurate description of the shear mechanics, the cross-section deformation, Poisson's effect along the spatial directions and the torsional mechanics in more detail than classical models do. Traditional kinematic assumptions of EBBM neglect them all, since this theory was formulated to describe the bending mechanics. TBM takes into account constant shear stress and strain components. According to the technique described by Carrera and Giunta (2010), opportunely reduced material stiffness coefficients are here adopted to correct Poisson's locking effect for classical theories and first-order models.

4. Finite element formulation

Following standard FEM, the unknown variables in the element domain are expressed in terms of their values corresponding to the element nodes (Carrera *et al*. 2011). For the sake of completeness, some details about the formulation of CUF finite elements are here retrieved from previous works (Carrera *et al*. 2012, Carrera and Varello 2012) and extended to the static analysis of nonhomogeneous structures. By introducing the shape functions N_i and the nodal displacement vector $\boldsymbol{q}$, the displacement field becomes:

$$\boldsymbol{u}(x,y,z) = F_\tau(x,z)\, N_i(y)\boldsymbol{q}_{\tau i} \qquad i = 1,2,\dots,N_N \tag{7}$$

where:

$$\boldsymbol{q}_{\tau i} = \left\{ q_{u_x \tau i} \quad q_{u_y \tau i} \quad q_{u_z \tau i} \right\}^T \tag{8}$$

contains the degrees of freedom of the τ^{th}expansion term corresponding to the i^{th}element node. 1D elements with N_N number of nodes equal to 2, 3 and 4 are formulated and named B2, B3, and B4, respectively. The results reported in the present work involve only B4 elements. Third-order Lagrange polynomials are used as shape functions (Bathe 1996). For the sake of brevity, more details are not reported here, but can be found in the work of Carrera *et al*. (2010).

As far as the number of DOFs is concerned, for instance $N = 2$ model leads to 6 unknowns for each displacement component u_x, u_y, u_z and then 18 DOFs per node, whereas the fifth-order model ($N = 5$) involves 21 unknowns per displacement component and 63 DOFs per node. The 1D CUF model can be easily extended to mixed theories. However, this work presents a displacement-based formulation. The variational statement is therefore the Principle of Virtual Displacements:

$$\delta L_{int} = \int_V \left(\delta \boldsymbol{\varepsilon}_n^T \boldsymbol{\sigma}_n + \delta \boldsymbol{\varepsilon}_p^T \boldsymbol{\sigma}_p \right) dV = \delta L_{ext} \tag{9}$$

where L_{int} is the internal strain energy and L_{ext} is the work of external loadings. δ stands for the virtual variation. Substituting Eq. (7) into Eq. (2) and using Eq. (3), the expression of the internal strain energy (Eq. (9)) can be rewritten in terms of virtual nodal displacements as follows:

$$\delta L_{int} = \delta \boldsymbol{q}_{\tau i}^T \; \boldsymbol{K}^{ij\tau s} \; \boldsymbol{q}_{sj} \tag{10}$$

The 3×3 *fundamental nucleus* of the structural stiffness matrix presented in Eq. (10) can be shown to have the following explicit equation:

$$\begin{aligned} \boldsymbol{K}^{ij\tau s} = {} & E_{ij} \lhd \left(\boldsymbol{D}_{np}^T \; F_\tau \boldsymbol{I} \right) \left[\boldsymbol{C}_{np} \left(\boldsymbol{D}_p \; F_s \boldsymbol{I} \right) + \boldsymbol{C}_{nn} \left(\boldsymbol{D}_{np} \; F_s \boldsymbol{I} \right) \right] + \\ & \left(\boldsymbol{D}_p^T F_\tau \boldsymbol{I} \right) \left[\boldsymbol{C}_{pp} \left(\boldsymbol{D}_p F_s \boldsymbol{I} \right) + \boldsymbol{C}_{pn} \left(\boldsymbol{D}_{np} F_s \boldsymbol{I} \right) \right] \rhd_\Omega + \\ & E_{ij\,,y} \lhd \left[\left(\boldsymbol{D}_{np}^T F_\tau \boldsymbol{I} \right) \boldsymbol{C}_{nn} + \left(\boldsymbol{D}_p^T F_\tau \boldsymbol{I} \right) \boldsymbol{C}_{pn} \right] F_s \rhd_\Omega \boldsymbol{I}_{\Omega \mathrm{y}} + \\ & E_{i\,,y\,j} \boldsymbol{I}_{\Omega \mathrm{y}}^T \lhd F_\tau \left[\boldsymbol{C}_{np} \left(\boldsymbol{D}_p F_s \boldsymbol{I} \right) + \boldsymbol{C}_{nn} \left(\boldsymbol{D}_{np} F_s \boldsymbol{I} \right) \right] \rhd_\Omega + \\ & E_{i\,,y\,j\,,y} \boldsymbol{I}_{\Omega \mathrm{y}}^T \lhd F_\tau \boldsymbol{C}_{nn} F_s \rhd_\Omega \boldsymbol{I}_{\Omega \mathrm{y}} \end{aligned} \tag{11}$$

where:

$$\boldsymbol{I}_{\Omega \mathrm{y}}=\begin{bmatrix}0 & 0 & 1\\ 1 & 0 & 0\\ 0 & 1 & 0\end{bmatrix} \qquad \lhd \ \ldots \ \rhd_{\Omega}=\int_{\Omega} \ldots \, d\Omega=\sum_{k}^{N_S}\int_{\Omega_k} \ldots \, d\Omega_k \tag{12}$$

$$\left(E_{ij},\, E_{ij,y},\, E_{i,yj},\, E_{i,yj,y}\right)=\int_{l} \left(N_iN_j,\, N_iN_{j,y},\, N_{i,y}N_j,\, N_{i,y}N_{j,y}\right) dy \tag{13}$$

In Eq. (11) $\boldsymbol{I}$ is the identity matrix. The integration over Ω can be performed numerically over an arbitrary cross-section and is indicated by the symbol $\lhd \ \ldots \ \rhd_{\Omega}$. For nonhomogeneous sections, the integral over Ω includes the contributions corresponding to each subsection as expressed in Eq. (12), where Ω_k is the k^{th} subsection. This method is consistent with the equivalent single-layer approach widely used for layered structures, where a homogenization of the material properties is conducted by summing the contributions of each layer in the stiffness matrix. For the sake of completeness, let the cross-section depicted in Fig. 1 with three subsections ($N_S = 3$) to be considered. In this particular case, the last integral term of Eq. (11) is computed via three contributions as follows:

$$\lhd F_\tau \boldsymbol{C}_{nn} F_s \rhd_{\Omega}=\int_{\Omega_1} F_\tau \boldsymbol{C}^1_{nn} F_s d\Omega_1 \ +\int_{\Omega_2} F_\tau \boldsymbol{C}^2_{nn} F_s d\Omega_2 \ +\int_{\Omega_3} F_\tau \boldsymbol{C}^3_{nn} F_s d\Omega_3 \tag{14}$$

Where Ω_1, Ω_2, and Ω_3 are subsections 1, 2 and 3. Shear locking is corrected through selective integration via a typical reduced Gauss integration (Bathe 1996) of the terms in Eq. (13) related to the transverse shear. Full integration is adopted for the other terms. The virtual work of external loadings variationally consistent with the above method is here derived for the case of a generic concentrated load $\boldsymbol{P}=\left\{P_{u_x} \ P_{u_y} \ P_{u_z}\right\}^T$ acting on the load application point $(x_P,\ y_P,\ z_P)$. By using Eq. (7), δL_{ext} becomes:

$$\delta L_{ext} \ = \ \delta \boldsymbol{u}^T \boldsymbol{P}=\delta \boldsymbol{q}^T_{\tau i} F_\tau N_i \boldsymbol{P}= \ \delta \boldsymbol{q}^T_{\tau i} \boldsymbol{F}_{\tau i} \tag{15}$$

where F_τ is evaluated in $(x_P,\ z_P)$ and N_i is calculated in y_P. Any other loading condition can be similarly treated. From Eqs. (9), (10), and (15) the system of equilibrium equations can be derived through a finite element assembly procedure:

$$\mathbf{Kq}=\mathbf{F} \tag{16}$$

where $\mathbf{K}$ is the structural stiffness matrix and $\mathbf{F}$ is the vector of equivalent nodal forces. It should be noted that no assumptions on the expansion order have been made so far. Therefore, it is possible to obtain variable kinematic 1D models without changing the formal expression of the nuclei components. Thanks to the CUF, the present model is invariant with respect to the order of the displacement field expansion and the type of finite elements used in the longitudinal axial discretization.

5. Numerical results and discussion

The ultimate aim of the present paper is the assessment of one-dimensional CUF models in the linear static analysis of structures with arbitrary cross-sections made of nonhomogeneous materials, as mentioned above. A three-layer circular cylindrical shell is considered as first test case with a

laminated conventional (annular) cross-section. Then, an atherosclerotic plaque is introduced as a typical structure with arbitrary cross-section geometry and studied for both the homogeneous and nonhomogeneous material cases through the present 1D higher-order models by comparison with 3D finite element solutions.

5.1 Annular cross-section made of nonhomogeneous material

A thin-walled cylinder with a nonhomogeneous cross-section is now introduced. As depicted in Fig. 2, the cross-section is composed of three thin circular layers denoted as layers 1, 2 and 3. The layers of the cylinder are made of three different isotropic materials, whose properties are summarized in Table 1. The thickness $t = 1$ mm is constant for each layer and is small enough to consider overall the cylinder as a thin-walled structure, since the external and internal diameters are equal to $d_e = 100$ mm and $d_i = 94$ mm, respectively. The length L of the cylinder is equal to 500 mm. A clamped boundary condition is taken into account for the edges of the cylinder at $y = 0$ and $y = L$.

In order to easily present the deformation of the cylinder, a cylindrical coordinate system $r - \theta - y$ is nowintroduced. The plane $r - \theta$ is the cross-section plane. The r coordinate goes along the radial direction, whereas the θ coordinate is an angle measured counterclockwise from the axis$-z$, see Fig. 2. For the sake of simplicity, the origin of the cylindrical system overlaps the cross-section center of mass as well as the origin of the cartesian coordinate system.

A uniform pressure $p = 14.8$ MPa is applied on the internal edge of the cylinder as shown in Fig. 2. In particular, the loading is applied along all the length of the structure and only on the upper side of layer 1 ($r = d_i/2,\ \pi/2 \leq \theta \leq 3\pi/2$). This sample case is retrieved from the work of Varello and Carrera (2012). Although the structure here analyzed is axisymmetric, its deformed configuration is not expected to be axisymmetric due to this particular loading distribution. Nevertheless, the solution will be symmetrical with respect to both $x = 0$ and $y = L/2$ planes. Given the solution's symmetry with respect to $y = L/2$ plane, the maximum deformation is placed on the section lying on this plane. This section is denoted as mid-span section from this point forward.

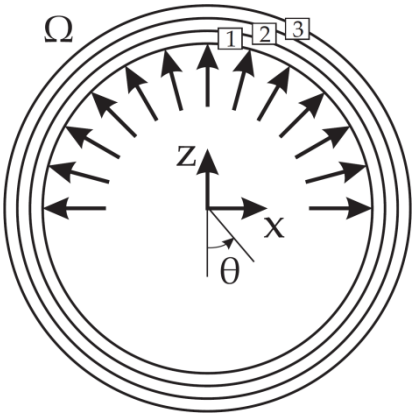

Fig. 2 Pressure applied to the cylinder with three different layers

Table 1 Material properties of the cylinder layers

Property	Layer 1	Layer 2	Layer 3
E [GPa]	69	30	15
ν	0.33	0.33	0.33

One-dimensional theories are usually employed to study slender beams because of their limiting kinematic hypotheses. Instead, the cylinder here considered is relatively short since the span-to-external diameter ratio L/d_e is equal to 5. Nevertheless, the static response of the structure is computed through the 1D CUF model with a variable expansion order up to $N = 8$ and a 1D mesh of 10 B4 finite elements by solving Eq. (16). A solid finite element analysis is also carried out via the commercial code NASTRAN and taken as reference in order to assess the present refined 1D model for a nonhomogeneous shell case. Due to the small layer thickness and the well-known aspect ratio restrictions typical of solid finite elements, the model in NASTRAN consists of 64800 HEX8 elements and 86880 nodes. The number of degrees of freedom (DOFs) is thus equal to 257760.

The deformation of the cylinder, which is expressed in terms of the magnitude of displacement vector $\boldsymbol{u}$ of the external edge of the annular mid-span section ($r = d_e/2,\ y = L/2$) along the angular θ coordinate, is depicted in Fig. 3 for different 1D models and compared with the solid NASTRAN solution. The solution confirms to be symmetrical with respect to the $x = 0$ plane regardless the model used. In addition to a bending behavior, the particular distribution of pressure loadings is supposed to deform the beam cross-section. This type of deformation cannot be consistent with the kinematic hypotheses of undeformed cross-section shape which classical beam models are based on. Classical models are therefore not expected to yield accurate results and this statement is confirmed by the constant displacement trend computed by Euler-Bernoulli beam theory. By enriching the displacement field, the first-order model provides a linear displacement distribution along the x and z directions, but it results not to be realistic. Taking the solid FE model as reference, the results obtained by the present formulation improve as the expansion order N increases. In particular, for an eighth-order model the deformation of the mid-span section is accurately described and its agreement with the 3D solution is remarkable. Even though it is not reported here, it is noteworthy that for an expansion order higher than 8 the analysis would provide the same results as those obtained by $N = 8$, thus confirming a convergent trend on N. However, for $N < 8$ the displacement is remarkably overestimated at point $\theta = \pi$ and dangerously underestimated at points where the displacement is actually maximum.

The maximum displacement on the external edge of the mid-span section is reported in Table 2. The error in computing the maximum deflection is significant for classical and low-order models, except for $N = 1$. Nonetheless, the solution for the first-order model is completely unrealistic, see Fig. 3. In general, u_{max} increases as N increases approaching the 3D value. Also the position of the maximum displacement along the external edge in terms of θ noticeably changes for different models. $\theta_{u_{max}}$ for 1D models with an expansion order higher than 4 coincides with the reference solution, whereas lower-order models show their low accuracy even in the position evaluation. This aspect has not to be underestimated because it turns out to be fundamental for a failure investigation, for instance. In conclusion, the eighth-order model proves its capability in detecting exactly the three-dimensional deformation of the layered thin-walled cylinder with a sizeable reduction in computational cost in terms of DOFs (4185 vs. 257760).

Table 2 Maximum displacement [mm] on the external edge of the mid-span section

Model	u_{max}	% Difference	$\theta_{u_{max}}$	DOFs
EBBM	5.639	-60.663	-	93
$N = 1$	14.272	-0.439	180	279
$N = 2$	8.780	-38.751	93	558
$N = 3$	12.011	-16.212	0	930
$N = 4$	12.625	-11.929	120	1395
$N = 5$	12.685	-11.510	117	1953
$N = 6$	13.281	-7.353	117	2604
$N = 7$	13.300	-7.220	117	3348
$N = 8$	14.236	-0.691	117	4185
Solid FEM	14.335	-	117	257760

5.2 Arterial cross-section with a pronounced atherosclerotic plaque

As previously indicated, the present hierarchical formulation is able to cope with arbitrary cross-section geometries as well as arbitrary material laminations. Once the capabilities of higher-order 1D CUF models have been assessed for the previous nonhomogeneous cylinder case with a classic annular section, a human external iliac artery with a pronounced atherosclerotic plaque is now considered as an important application in biomechanics of an arbitrary cross-section structure. In particular, a portion of the atherosclerotic artery with a severe stenoses (lumen reduction) presented by Holzapfel *et al*. (2004) is introduced.

The components of the artery are identified by hrMRI (high resolution magnetic resonance imaging) and histological analysis (Holzapfel *et al*. 2004), see Figs. 4(a) and 4(b). These approaches consider eight different tissue types: fibrous cap (FC), i.e., the fibrotic part at the luminal border, calcification (C), lipid pool (LP), adventitia (A), non-diseased media (M), non-diseased intima, fibrotic intima at the medial border and diseased fibrotic media. As done by Balzani *et al*. (2012), for the following numerical investigations the non-diseased intima is neglected. Furthermore, the fibrotic intima at the medial border and the diseased fibrotic media are treated as one component, the fibrotic media (FM). According to these assumptions, in the work of Balzani *et al*. (2012) the same cross-section including the above mentioned components is discretized with 6048 triangular elements with quadratic Ansatz functions, as depicted in Fig. 4(c).

The section width and height of the cross-section are approximately the same and equal to 20 mm. For the sake of simplicity, the arterial cross-section is extruded along the out-of-plane direction (y axis) for 40 mm. A clamped boundary condition is taken into account for the edges at $y = 0$ and $y = L$. These constraints provide a particularly strict condition for the assessment of the present 1D CUF model, as they provide a remarkable variation along the longitudinal direction of the cross-section deformation which is even more tricky to be accurately detected by a 1D reduced order model. The structure is here modeled with a one-dimensional mesh of 10 B4 finite elements (31 nodes), as shown in Fig. 5(c), and analyzed through the CUF formulation. Furthermore, a FE model is built in NASTRAN and discretized with a mesh of 244320 HEX8 solid elements (260172 nodes) with a total number of DOFs equal to 761244. Figs. 5(a) and 5(b) show the solid model of the atherosclerotic plaque, obtained by extruding the same cross-section shape as that used by Balzani *et al*. (2012) (see Fig. 4(c)). The linear static analysis is performed with a uniform pressure load of 180 mmHg ($\cong$ 24 kPa) applied on the surface bounding the lumen, i.e., the inside space of the artery, as illustrated in Fig. 5(a). This pressure level may be seen as an upper bound for the hypertensive internal blood pressure.

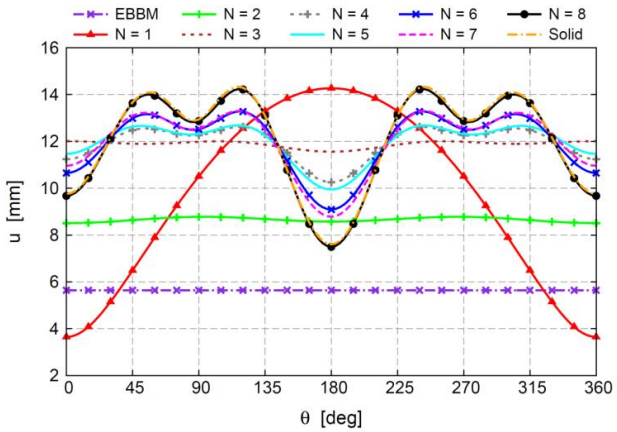

Fig. 3 Displacement of the external edge of the mid-span section. Layered cylinder case

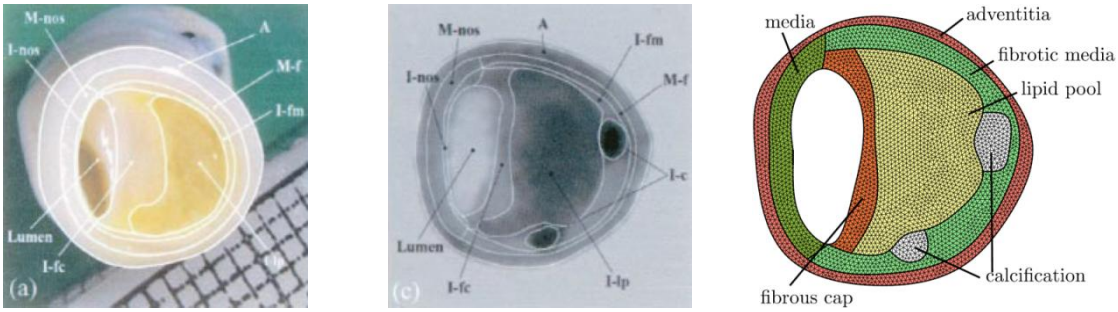

(a) Segmented macroscopic view (Holzapfel *et al*. 2004)

(b) High resolution magnetic resonance image (hrMRI) (Holzapfel *et al*. 2004)

(c) Two-dimensional model used by (Balzani *et al*. 2012)

Fig. 4 Arterial cross-section with a pronounced atherosclerotic plaque in a human external iliac artery

(a) Solid model: cross-section under uniform internal blood pressure

(b) Solid model: three-dimensional view

(c) Mesh of the one-dimensional model

Fig. 5 Simplified solid model of the arterial atherosclerotic plaque discretized with 244320 HEX8 solid finite elements in NASTRAN (a), (b). Mesh of the one-dimensional CUF model discretized with 10 B4 finite elements(c). Homogeneous material case

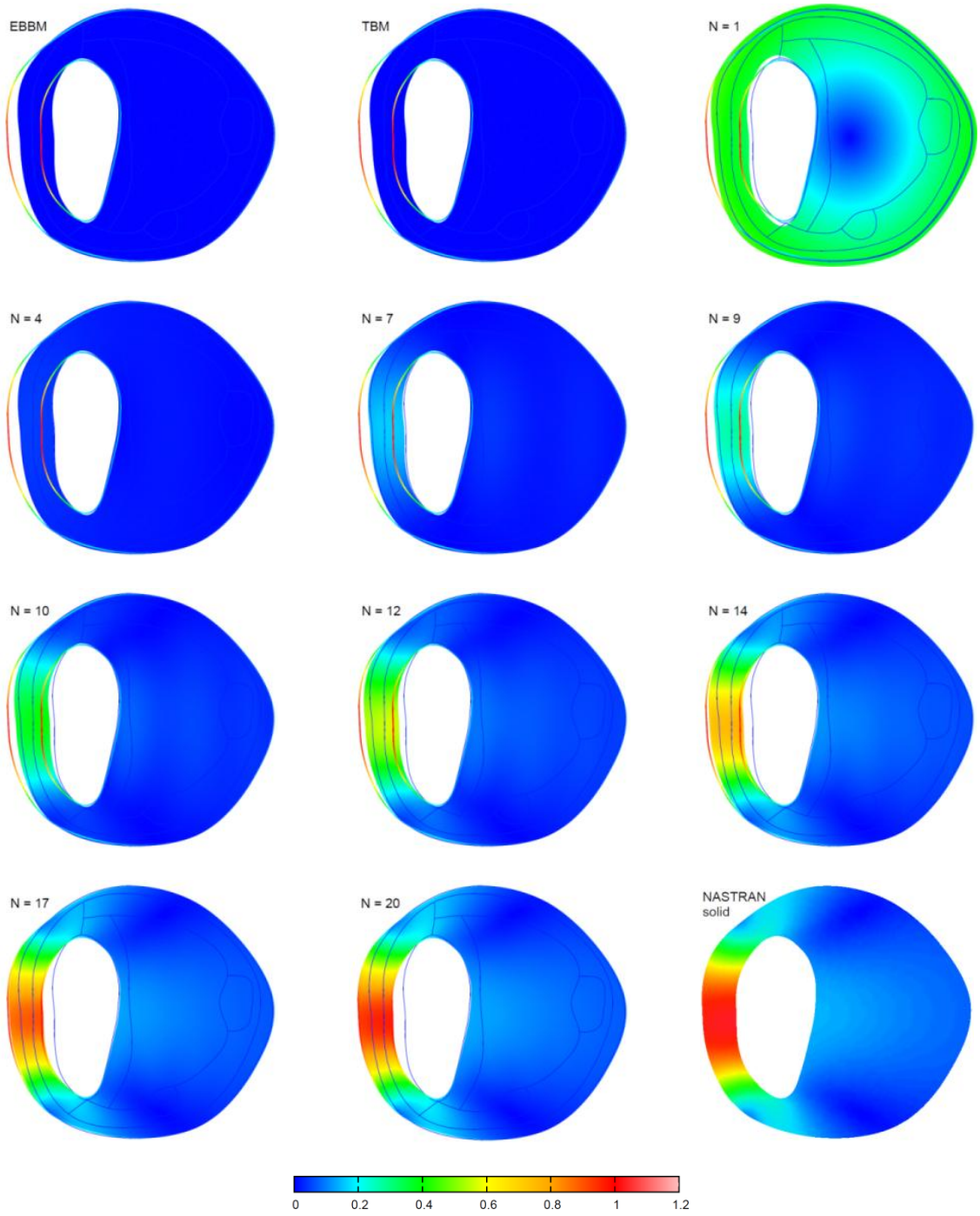

Fig. 6 Displacement $|\boldsymbol{u}|$ [mm] over the mid-span cross-section of the atherosclerotic plaque for different one-dimensional models compared to the solid FE solution. Homogeneous material case

Higher-order CUF models with a variable expansion order N are employed and the results are compared to the solid FEM solution. Both the cases of homogeneous and nonhomogeneous materials are considered and afterwards described. The clinic application above described is a very preliminary application of the 1D CUF model to the study of a biomechanical case. For the sake of completeness, it is emphasized that the following results provide a numerical example of limited validity with respect to quantitative results. However, this section has the goal to show that the proposed one-dimensional CUF models provide an excellent agreement with a three-dimensional solution in the context of finite element simulations, with a remarkable reduction in computational cost (in terms of DOFs).

5.2.1 Homogeneous material case

A simplified test case is here addressed by assuming the cross-section made of homogeneous isotropic material. Averaging grossly the Young's moduli of the six arterial tissue types reported by Balzani *et al*. (2012), the Young's modulus considered is $E = 2.4$ MPa and Poisson's ratio is $\nu = 0.33$. Fig. 6 shows the deformation of the mid-span arterial cross-section ($y = L/2$), where the maximum displacement is located, for different one-dimensional models (up to $N = 20$) compared to the solid FE solution. In particular, the colored map of each subfigure represents the magnitude of the displacement vector $\boldsymbol{u}$ computed over the section by each one-dimensional theory. On the contrary, the two colored curves show the internal and external plaque contours in the deformed configuration computed through the solid FE method, which is taken as reference. The remaining blue lines are the edges of the six arterial issues.

As expected, classical beam theories (EBBM and TBM) are completely not able to study this case due to their kinematic hypotheses about the cross-section deformation. In fact, they show a uniform quasi-null displacement over the cross-section. The first-order model ($N = 1$) enables the in-plane deformation of the cross-section but the result is again completely wrong with respect to the 3D solution. In this case, even low-order theories are not accurate enough to catch an acceptable solution compared to the 3D simulation. According to the reference solid solution, the reason is that the plaque deforms locally around the lumen, i.e., the load application region, whereas a quasi-null displacement is observed far from the lumen. This particular deformation requires a high expansion order for the present formulation to reach an acceptable accuracy. In particular, the tissues most interested by the internal blood pressure are the media and the part of adventitia in contact with the media. Though surrounding part of the lumen and being thus directly loaded by the pressure, the fibrous cap is barely deformed and its maximum displacement is placed close to the media. As will be seen in the nonhomogeneous material case, this fact is directly related to the assumption of homogeneous material for all the tissue types. In fact, when a homogeneous material is taken into account the volume occupied by the lipid pool and calcification remarkably stiffens the side of the section on the right of the lumen with respect to the left one.

Despite its one-dimensional approach, the proposed higher-order model is able to accurately detect the in-plane deformation of this kind of cross-section with arbitrary geometry. In fact, the proposed 1D FEs provide a convergent solution by approaching the NASTRAN 3D results as the refinement of the expansion increases, until a well agreement is achieved for $N = 20$. As can be seen in Fig. 6, the region subjected to the maximum displacement lies on the central part of media (M) and adventitia (A). Thus, the maximum displacements on media and adventitia computed by the different models are reported in Table 3 and indicated as u_{max}^{M} and u_{max}^{A}, respectively. For the sake of completeness, also the maximum displacement on fibrous cap u_{max}^{FC} is reported, even

though it is much lower as previously mentioned. As expected, classical beam theories are completely ineffective in studying this kind of structure, giving a constant quasi-null displacement over the section. For all the displacements summarized, the increase of the expansion order N improves the results approaching the reference data with a convergent trend. In fact, the introduction of higher-order terms enables the structure to deform in a more realistic way and results to be fundamental in order to catch properly the artery deformation. It is important to note the remarkably lower computational effort required by 1D CUF model. In fact, the $N = 20$ model provides an acceptable maximum error but with a number of degrees of freedom equal to 21483, about 35 times slower than the DOFs required by the solid FE model.

Numerical results are presented also for strain and stress quantities in Table 4. In particular, the maximum value of the transverse normal strain ε_{zz}^{max}, the minimum (negative) value of the longitudinal normal strain ε_{yy}^{min}, and the maximum value of the transverse normal stress σ_{zz}^{max} (all lying in the adventitia) are reported for different one-dimensional models in comparison with the three-dimensional solution. The reason of this choice is to compare the 1D higher-order formulation with classical beam theories, which neglect ε_{zz} and σ_{zz} by definition. For the arterial case studied, higher-order models highlight that these transverse quantities are not negligible in agreement with 3D results. Moreover, although EBBM and TBM take into account the longitudinal normal strain ε_{yy}, Table 4 shows that even this quantity is completely wrongly computed by classical beam theories, which in this case are able to catch only a uniform quasi-null displacement, see Fig. 6 and Table 3. In general, the convergent trend obtained for displacements as N increases occurs also for strain and stress computation, approaching the reference 3D results with a remarkably lower number of DOFs.

Table 3 Maximum displacements [mm] on media, adventitia and fibrous cap of the atherosclerotic plaque over the mid-span cross-section for different models. Homogeneous material case

Model	u_{max}^{M}	(% Error)	u_{max}^{A}	(% Error)	u_{max}^{FC}	(% Error)	DOFs
EBBM	0.0000	(-100.00%)	0.0000	(-100.00%)	0.0000	(-100.00%)	93
TBM	0.0001	(-99.99%)	0.0001	(-99.99%)	0.0001	(-99.95%)	155
$N = 1$	0.4212	(-58.88%)	0.4632	(-53.96%)	0.3656	(+93.44%)	279
$N = 4$	0.0468	(-95.43%)	0.0471	(-95.32%)	0.0263	(-86.08%)	1395
$N = 7$	0.1631	(-84.08%)	0.1609	(-84.01%)	0.0402	(-78.73%)	3348
$N = 9$	0.2774	(-72.92%)	0.2674	(-73.42%)	0.0569	(-69.89%)	5115
$N = 10$	0.3999	(-60.96%)	0.3839	(-61.84%)	0.0770	(-59.26%)	6138
$N = 12$	0.5696	(-44.39%)	0.5469	(-45.64%)	0.0912	(-51.75%)	8463
$N = 14$	0.7628	(-25.53%)	0.7468	(-25.77%)	0.1322	(-30.05%)	11160
$N = 17$	0.9001	(-12.13%)	0.8884	(-11.70%)	0.1581	(-16.35%)	15903
$N = 19$	0.9441	(-7.83%)	0.9320	(-7.36%)	0.1661	(-12.12%)	19530
$N = 20$	0.9645	(-5.84%)	0.9537	(-5.21%)	0.1714	(-9.31%)	21483
NASTRAN solid	1.0243	-	1.0061	-	0.1890	-	761244

Table 4 Some maximum and minimum strain and stress [MPa] values on the atherosclerotic plaque over the mid-span cross-section for different models. Homogeneous material case

Model	$10^2\varepsilon_{zz}^{max}$	(% Error)	$10^2\varepsilon_{yy}^{min}$	(% Error)	σ_{zz}^{max}	(% Error)	DOFs
EBBM	0.0000	(-100.00%)	-0.0004	(-99.86%)	0.00	(-100.00%)	93
TBM	0.0000	(-100.00 %)	-0.0004	(-99.86%)	0.00	(-100.00 %)	155
$N = 1$	3.7706	(-52.97%)	-0.0004	(-99.86 %)	0.00	(-100.00 %)	279
$N = 4$	0.6539	(-91.84%)	-0.0421	(-85.39%)	31.40	(-85.68%)	1395
$N = 7$	1.4728	(-81.63%)	-0.0505	(-82.47%)	59.53	(-72.86%)	3348
$N = 9$	2.3757	(-70.37%)	-0.0736	(-74.45%)	110.60	(-49.57%)	5115
$N = 10$	3.3719	(-57.94%)	-0.1045	(-63.73%)	112.31	(-48.79%)	6138
$N = 12$	4.7096	(-41.25%)	-0.1453	(-49.57%)	134.44	(-38.70%)	8463
$N = 14$	6.2810	(-21.65%)	-0.1997	(-30.68%)	184.00	(-16.10%)	11160
$N = 17$	7.1202	(-11.18%)	-0.2382	(-17.32%)	200.49	(-8.58%)	15903
$N = 19$	7.5109	(-6.31%)	-0.2514	(-12.74%)	194.66	(-11.24%)	19530
$N = 20$	7.7067	(-3.87%)	-0.2590	(-10.10%)	204.56	(-6.73%)	21483
NASTRAN solid	8.0169	-	-0.2881	-	219.31	-	761244

In addition to the evaluation of the maximum value of σ_{zz}, a comparison of this transverse normal stress between the model $N = 20$ and the 3D reference solution is presented in Fig. 7. The figure clearly shows that the σ_{zz}^{max} value is obtained in the adventitia of the mid-span atherosclerotic plaque and that the internal blood pressure causes a stress field locally influenced on the left of the lumen. It is important to remark the accuracy achieved by the 1D twentieth-order model in detecting the stress field all over the cross-section, reaching with a much lower computational cost (21438 vs. 761244 DOFs) an approximation comparable to the three-dimensional model. It is noteworthy that higher-order terms are necessary for the proper evaluation of all transverse normal and shear strains and stresses, which is a feature not present in standard beam models. A more accurate comparison of strain and stress terms over the structure will be carried out in the following nonhomogeneous material case.

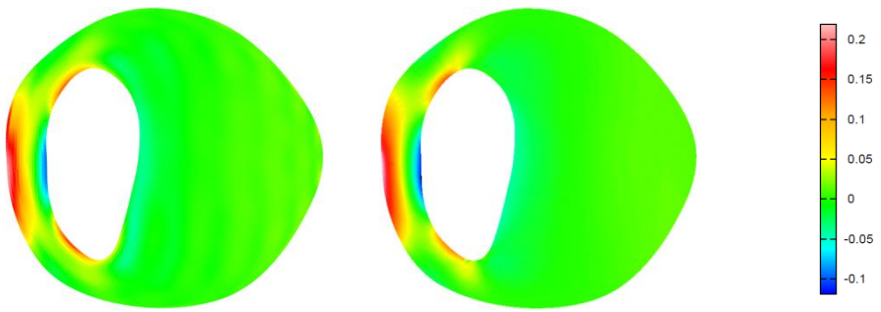

$N = 20$ NASTRAN solid

Fig. 7 Comparison of stress σ_{zz} [MPa] over the mid-span cross-section of the atherosclerotic plaque between the present $N = 20$model (21483 DOFs) and NASTRAN solid model (761244 DOFs). Homogeneous material case

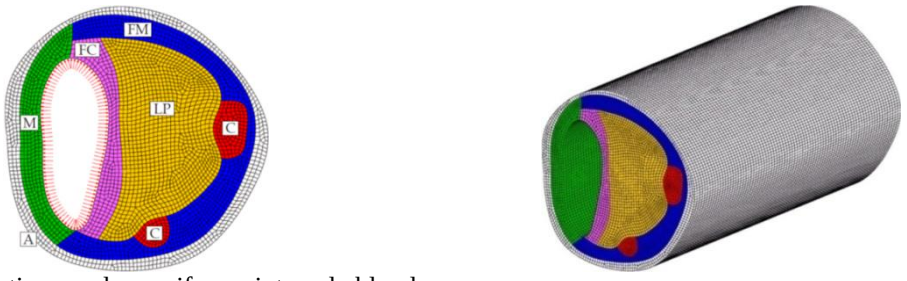

(a) Cross-section under uniform internal blood pressure

(b) Three-dimensional view

Fig. 8 Simplified solid model of the arterial atherosclerotic plaque discretized with 64800 solid HEX8 finite elements in NASTRAN. Nonhomogeneous material case

5.2.2 Nonhomogeneous material case

The assessment procedure on the simplified case of homogeneous atherosclerotic plaque is completed. The same static analysis is carried out now considering a different material for each of the six tissues constituting the atherosclerotic plaque. As illustrated in Fig. 8, the mesh of the solid finite element model is the same as that employed for the analysis of the homogeneous material case (in Fig. 5). In Balzani *et al*. (2012) the calcification is assumed to be isotropic and the lipid pool is a neo-Hookean material.

The adventitia, media, fibrous cap, fibrotic media are instead modeled as hyperelastic materials defined via several hyperelastic and damage parameters. For the sake of simplicity, all the six tissues of Fig. 8(a) are here assumed to be made of linear isotropic materials. The isotropic material properties of each tissue are introduced extrapolating grossly the Young's moduli used by Balzani *et al*. (2012) and reported in Table 5 with the corresponding acronyms. It is important to note that this approximation is not very relevant for the purpose of this work, i.e., the assessment of the 1D formulation with respect to a solid FE model in presence of significant nonhomogeneities. In fact, it is emphasized that the following results provide a numerical example of limited validity with respect to quantitative results.

Also for the nonhomogeneous case, the displacements computed by 1D CUF models over the mid-span cross-section are depicted in Fig. 9 and compared with a commercial solid finite element solution (NASTRAN). The equivalent results of the homogeneous case have been presented in Fig. 6. Comparing Figs. 6 and 9, it points out that now the deformation of the cross-section, under the same internal blood pressure, is higher than the deformation obtained in the homogeneous case. In fact, when each tissue is modeled through a different material, the large volume occupied by the lipid pool is very deformable and “relaxes” the in-plane cross-section rigidity. The lipid pool deforms significantly as well as the fibrous cap, unlike for the homogeneous case. As a consequence, also the adventitia and the media present displacement values higher than the previous case. Nonetheless, the deformation of the calcification and fibrotic media remains quasi-null due to their high material stiffness. In general, this larger in-plane cross-section deformation requires an expansion order higher than the homogeneous case to obtain a good agreement with the solid finite element solution, which is achieved with $N = 22$. It is noteworthy that even for this very complex structure made of nonhomogeneous material with arbitrary cross-section geometry, the more the expansion order N is, the more the results obtained through the 1D formulation are accurate, approaching the NASTRAN results.

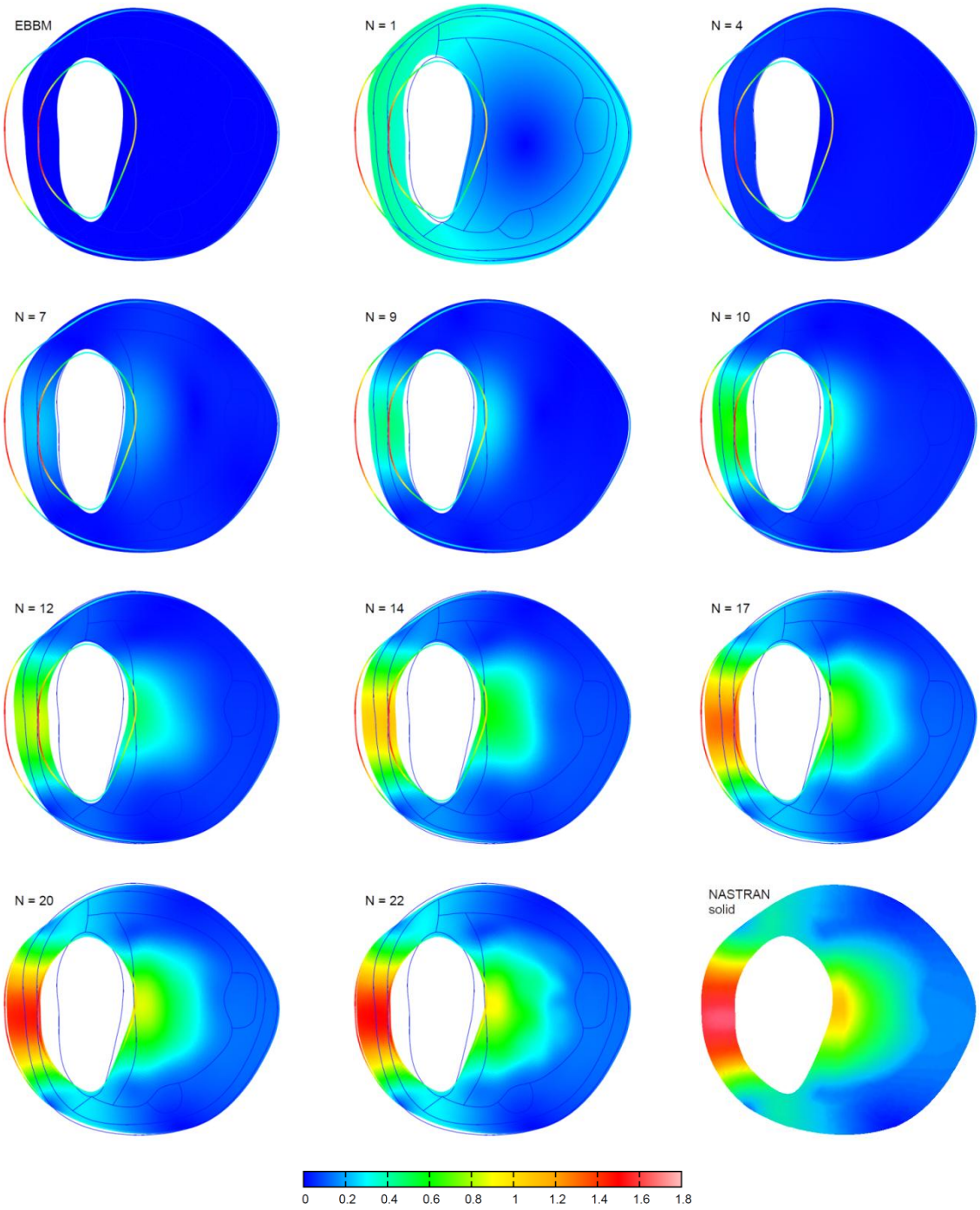

Fig. 9 Displacement $|\boldsymbol{u}|$ [mm] over the mid-span cross-section of the atherosclerotic plaque for different one-dimensional models compared to the solid FE solution. Nonhomogeneous material case

Table 5 Material properties of the tissue types used for the analysis of the arterial atherosclerotic plaque Nonhomogeneous material case

Tissue type	E [MPa]	ν
Calcification (C)	12	0.33
Lipid pool (LP)	0.1	0.33
Fibrous cap (FC)	2.4	0.33
Media (M)	1	0.33
Fibrotic media (FM)	5	0.33
Adventitia (A)	2.5	0.33

Table 6 Maximum displacements [mm] on media, adventitia and fibrous cap of the atherosclerotic plaque over the mid-span cross-section for different models. Nonhomogeneous material case

Model	u_{max}^{M}	(% Error)	u_{max}^{A}	(% Error)	u_{max}^{FC}	(% Error)	DOFs
EBBM	0.0000	(-100.00 %)	0.0000	(-100.00 %)	0.0000	(-100.00 %)	93
TBM	0.0001	(-99.99 %)	0.0001	(-99.99 %)	0.0001	(-99.95 %)	155
$N = 1$	0.4200	(-74.31 %)	0.4590	(-71.68 %)	0.3552	(-65.65 %)	279
$N = 4$	0.0713	(-95.64 %)	0.0716	(-95.58 %)	0.0515	(-95.02 %)	1395
$N = 7$	0.2333	(-85.73 %)	0.2329	(-85.63 %)	0.2075	(-79.94 %)	3348
$N = 9$	0.4556	(-72.13 %)	0.4435	(-72.64 %)	0.2922	(-71.75 %)	5115
$N = 10$	0.6430	(-60.67 %)	0.6176	(-61.89 %)	0.3496	(-66.20 %)	6138
$N = 12$	0.8491	(-48.06 %)	0.8102	(-50.01 %)	0.4740	(-54.17 %)	8463
$N = 14$	1.0911	(-33.26 %)	1.0611	(-34.53 %)	0.6125	(-40.77 %)	11160
$N = 17$	1.3249	(-18.96 %)	1.3122	(-19.04 %)	0.7826	(-24.33 %)	15903
$N = 20$	1.4650	(-10.39 %)	1.4575	(-10.08 %)	0.8649	(-16.37 %)	21483
$N = 21$	1.4855	(-9.14 %)	1.4804	(-8.66 %)	0.8714	(-15.74 %)	23529
$N = 22$	1.5047	(-7.96 %)	1.4928	(-7.90 %)	0.9194	(-11.10 %)	25668
NASTRAN solid	1.6349	-	1.6208	-	1.0342	-	761244

The same maximum results over the cross-section as those presented in Table 3 are now reported for the nonhomogeneous case in Table 6. The analysis involves models with N up to 22 and shows the larger deformation due to the nonhomogeneous material. Whereas about a 60 percent increase is observed in u_{max}^{M} and u_{max}^{A}, the maximum displacement in the fibrous cap u_{max}^{FC} shows about a 450 percent increase,mainly due to the butter-like behavior of the lipid pool. The considerations about the inefficiency of classical beam theories made for the homogeneous case are still valid here. On the contrary, the 1D CUF FEs provide again a convergent solution by approaching the NASTRAN 3D results and a good agreement is obtained for $N = 22$. Although the error computed with respect to the 3D solution is about 8-11%, it is important to note that this error is on the overall maximum displacement values and that this approximation is achieved via about a 96% reduction in degrees of freedom (see Table 6).

Despite its one-dimensional approach, the proposed higher-order model is able to accurately detect the in-plane deformation of the cross-section even for this kind of cross-section made of nonhomogeneous material. A thorough assessment on strain and stress fields over the mid-span cross-section is now carried out. The two transverse normal strains ε_{xx} and ε_{zz} and the shear stress ε_{xz} are evaluated for the six arterial tissues and the relative maps are depicted on the deformed configuration in Figs. 10, 11, and 12, respectively. These strain quantities are related to

the beam cross-section, i.e., the components of vector $\boldsymbol{\varepsilon}_p$, and are neglected by classical beam theories. Considering the mid-span cross-section, the maximum values of these strains are achieved in the adventitia and media, whereas the minimum ones occur in the lipid pool and media. This fact clearly highlights the complexity of the case studied, given the markedly material nonhomogeneity. In fact, as can be seen also in Fig. 9, unlike the homogeneous material case, the whole section is affected by the internal blood pressure. Nonetheless, for all the strains mentioned, an expansion order equal to 21 provides a solution in excellent agreement with the reference 3D results. In general, a further increase of N might be required to achieve an even better accuracy, consistent with the considerations previously mentioned about the expansion enrichment.

Table 7 Some maximum and minimum strain and stress [MPa] values on the atherosclerotic plaque over the mid-span cross-section for different models. Nonhomogeneous material case

Model	$10^2\varepsilon_{zz}^{max}$	(% Error)	$10^2\varepsilon_{zz}^{min}$	(% Error)	σ_{zz}^{max}	(% Error)	DOFs
EBBM	0.000	(-100.00 %)	0.000	(-100.00 %)	0.00	(-100.00 %)	93
TBM	0.000	(-100.00 %)	0.000	(-100.00 %)	0.00	(-100.00 %)	155
$N = 1$	3.025	(-72.31 %)	3.025	(-129.94 %)	0.00	(-100.00 %)	279
$N = 4$	1.050	(-90.39 %)	-0.468	(-95.37 %)	42.04	(-86.51 %)	1395
$N = 7$	2.097	(-80.80 %)	-0.472	(-95.33 %)	74.70	(-76.03 %)	3348
$N = 9$	3.629	(-66.78 %)	-1.259	(-87.54 %)	162.98	(-47.70 %)	5115
$N = 10$	4.953	(-54.66 %)	-2.567	(-74.59 %)	171.68	(-44.91 %)	6138
$N = 12$	6.206	(-43.19 %)	-4.889	(-51.61 %)	179.47	(-42.41 %)	8463
$N = 14$	8.032	(-26.47 %)	-6.587	(-35.54 %)	228.49	(-26.68 %)	11160
$N = 17$	9.287	(-14.99 %)	-8.173	(-19.11 %)	274.38	(-11.95 %)	15903
$N = 20$	10.301	(-5.70 %)	-9.014	(-10.79 %)	287.15	(-7.86 %)	21483
$N = 21$	10.569	(-3.25 %)	-9.114	(-9.80 %)	311.23	(-0.13 %)	23529
NASTRAN solid	10.924	-	-10.104	-	311.63	-	761244

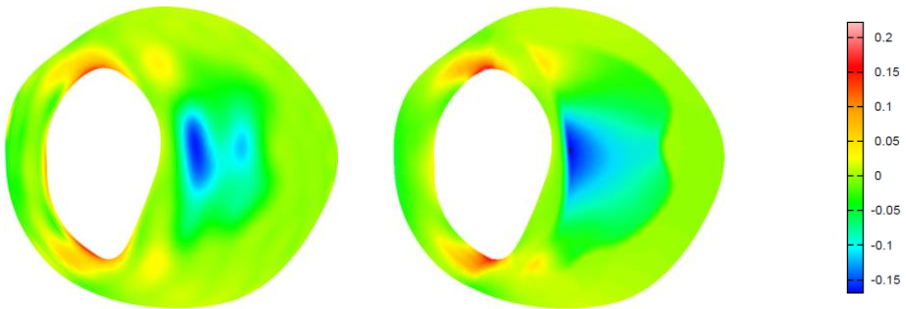

$N = 20$ NASTRAN solid

Fig. 10 Comparison of strain ε_{xx} over the mid-span cross-section of the atherosclerotic plaque between the present $N = 21$ model (23529 DOFs) and NASTRAN solid model (761244 DOFs). Nonhomogeneous material case

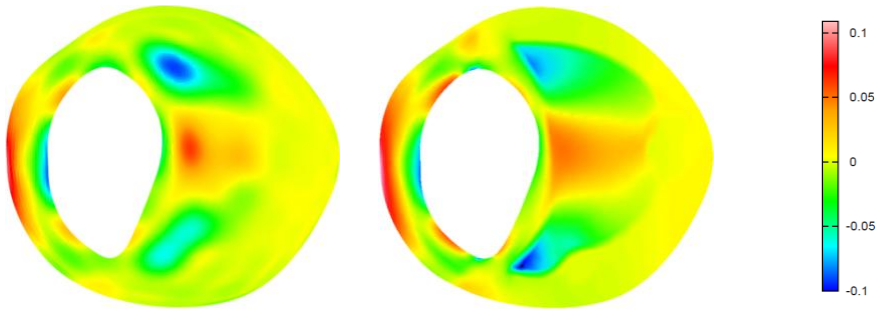

$N = 21$ NASTRAN solid

Fig. 11 Comparison of strain ε_{zz} over the mid-span cross-section of the atherosclerotic plaque between the present $N = 21$ model (23529 DOFs) and NASTRAN solid model (761244 DOFs). Nonhomogeneousmaterialcase

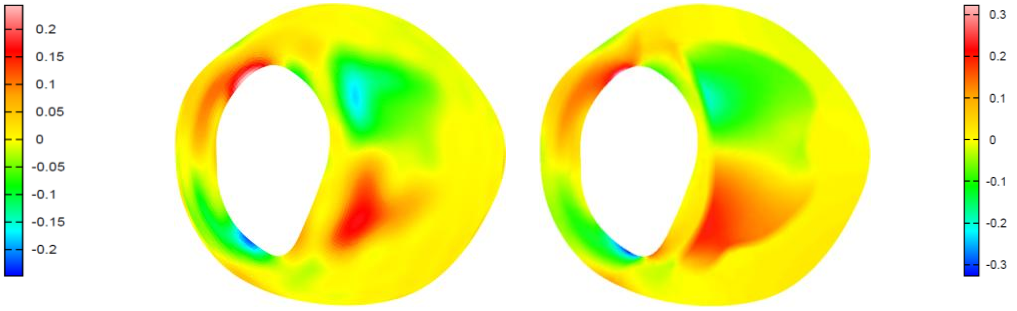

$N = 21$ NASTRAN solid

Fig. 12 Comparison of strain ε_{xz} over the mid-span cross-section of the atherosclerotic plaque between the present $N = 21$ model (23529 DOFs) and NASTRAN solid model (761244 DOFs). Nonhomogeneous material case

Numerical results for the transverse normal strain ε_{zz} are summarized in Table 7. In particular, the maximum value, lying in the adventitia, and the minimum value, lying in the lipid pool, are reported for different one-dimensional models up to $N = 21$and compared to the reference solution. As can be seen, classical and low-order models provide a unrealistic behavior of the arterial plaque. In fact, EBBM and TBM neglect ε_{zz}, whereas $N = 1$ takes into account an inaccurate non-null constant strain distribution. On the contrary, the proposed 1D FEs provide a convergent solution by approaching the NASTRAN 3D results as the refinement of the expansion increases. According to Fig. 11, a good agreement is achieved via a remarkably lower number of DOFs. The maximum value of the corresponding transverse normal stress σ_{zz}^{max} computed through an increasing expansion order is also presented in Table 7. The accuracy obtained demonstrates once again the three-dimensional capabilities of the CUF higher-order approach in computing the displacement and strain fields, since all the different strain terms are involved in the computation of stresses via the constitutive equations (Eq. (3)). These capabilities are nonstandard

for a one-dimensional formulation.

Figs. 13 and 14 compare the longitudinal stress σ_{yy} and the transverse normal stress σ_{zz} computed by the CUF model to the three-dimensional solution, respectively. The stress maps are depicted on the deformed configuration of the media, which is particularly stressed and subjected to both traction and compression. Even though the EBBM and TBM results are not reported here, it can be demonstrated that these classical beam theories are again completely ineffective for this case even in evaluating the axial stress, which is not neglected by kinematic hypotheses. Obviously, Figs. 13 and 14 show that the introduction of higher-order terms is fundamental not only for the accurate evaluation of the deformation, but also of the stress field. In fact, the higher the theory order employed the more the results approach the solid FEM solution with a convergent trend.

The present model allows the computation of strain and stress fields in every point of the structure analyzed. The shear stress σ_{xz} distribution over the cross-section is investigated with an expansion order equal to 21 and compared with the solid FE solution, bearing in mind that EBBM and TBM completely neglect it. The prediction of the shear stress σ_{xz} is slightly underestimated by the $N = 21$ model as can be noted by the different scales used in Fig. 15, but its distribution is well-detected all over the cross-section with an acceptable approximation with respect to the 3D solution, which involves a number of DOFs about 32 times higher.

In conclusion, the one-dimensional CUF formulation provides not only a correct evaluation of the displacements of the structure, but also a proper computation of the strain and stress fields. The atherosclerotic plaque studied here represents a very severe test case for the present one-dimensional model, from different points of view. First of all, this configuration is very short, given that the ratio between the length L and the characteristic cross-section dimension is about equal to 2. Furthermore, the cross-section has an arbitrary nonconventional geometrical layout. The material employed is markedly nonhomogeneous and, finally, the internal pressure load is applied on a nonplanar surface again of arbitrary geometry.

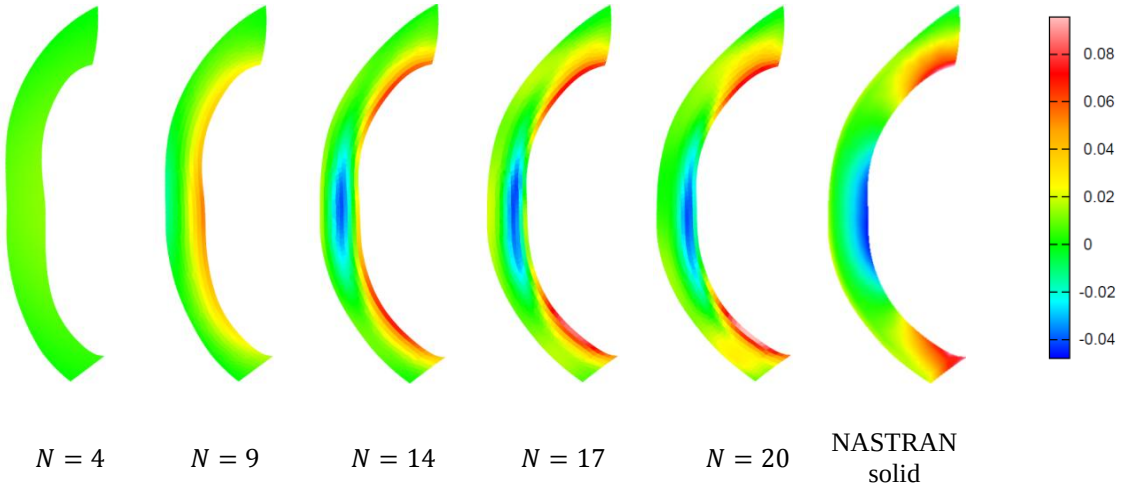

Fig. 13 Comparison of stress σ_{yy} [MPa] over the media of the atherosclerotic plaque (mid-span cross-section) for different models. Nonhomogeneous material case

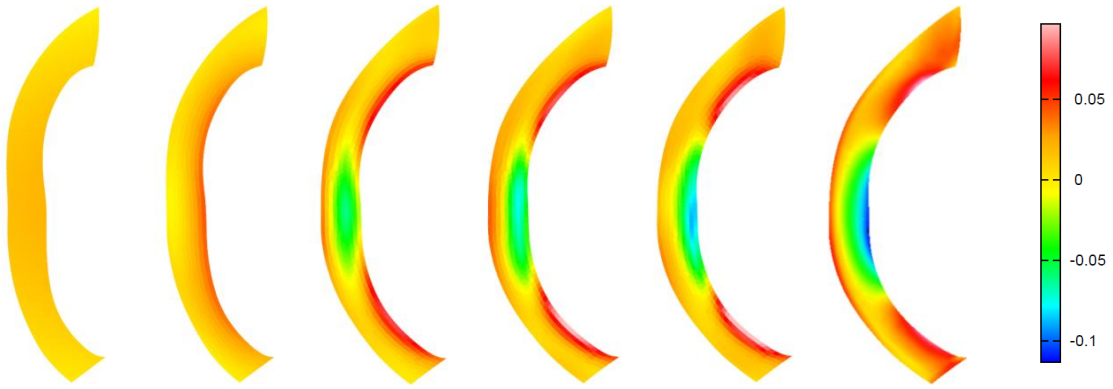

Fig. 14 Comparison of stress σ_{zz} [MPa] over the media of the atherosclerotic plaque (mid-span cross-section) for different models. Nonhomogeneous material case

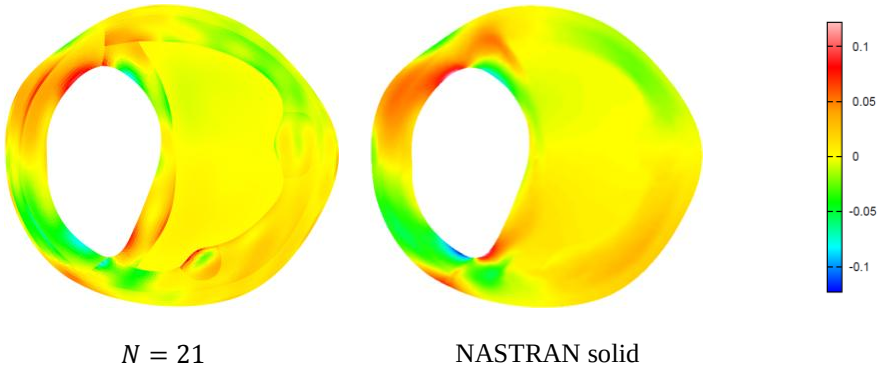

Fig. 15 Comparison of stress σ_{xz} [MPa] over the mid-span cross-section of the atherosclerotic plaque between the present $N = 21$ model (23529 DOFs) and NASTRAN solid model (761244 DOFs). Nonhomogeneous material case

6. Conclusions

The static analysis of structures with arbitrary cross-section geometries and materials through refined one-dimensional models is addressed in this paper. Variable kinematic 1D finite elements were formulated on the basis of Carrera Unified Formulation (CUF) and assessed by comparison with solid finite element solutions. As far as the use of 1D higher-order models is concerned, the following main conclusions can be drawn:

1. the introduction of higher-order terms in the displacement field is important even for the analysis of structures with conventional cross-sections. Higher-order models are required especially for structures with significant material nonhomogeneity and arbitrary geometry;

2. classical beam theories were completely ineffective in studying the kind of structures considered. Although Euler-Bernoulli's and Timoshenko's are basically bending beam theories, they were not able to accurately detect even the axial strain and stress, which are not neglected by the kinematic hypotheses of undeformed cross-section shape they are based on;
3. a convergent trend of displacement, strain and stress values approaching the three-dimensional results as the expansion order increases is achieved. This proves that the proposed 1D hierarchical model does not introduce additional numerical problems in the analysis of arbitrary nonhomogeneous structures with respect to classical beam theories.

As far as the present hierarchical one-dimensional approach is concerned, the results point out that:

a. CUF is the ideal tool to easily compare different higher-order theories. The expansion order of the model, i.e., its accuracy, is a free parameter of the analysis by exploiting a systematic procedure that leads to governing FE matrices whose form does not depend on the order of expansion used for the displacement unknowns over the cross-section;
b. in-plane cross-section deformations are well-described by the present 1D CUF models. The enrichment of the displacement field enables the structure to deform in a more realistic way and a very good agreement with the three-dimensional solution was achieved;
c. despite its one-dimensional approach, the proposed higher-order formulation proved its accuracy in the analysis of even short structures made of homogeneous or nonhomogeneous materials with classical or arbitrary cross-section geometries. Local effects and complete three-dimensional displacement, strain and stress fields were computed in well agreement with those obtained by three-dimensional models;
d. the refined 1D CUF model shows a remarkable reduction in computational cost in terms of DOFs with respect to the solid FE model.

Comparing results with three-dimensional solutions, the present 1D finite element formulation proved to be a valid alternative to shell and solid methods, which necessarily require a higher computational cost, and a promising numerical tool for the analysis of arbitrary nonhomogeneous structures in biomechanical applications. In this respect, further work should be done in order to take into account material anisotropy and nonlinearity typical of biological soft tissues.

References

Balzani, D., Brinkhues, S. and Holzapfel, G.A. (2012), "Constitutive framework for the modeling of damage in collagenous soft tissues with application to arterial walls", *Comput. Method. Appl. M.*, **213-216**, 139-151.

Bathe, K. (1996), *Finite element procedures*, Prentice Hall, Upper Saddle River, New Jersey.

Capelli, C., Gervaso, F., Petrini, L., Dubini, G. and Migliavacca, F. (2009), "Assessment of tissue prolapse after balloon-expandable stenting: influence of stent cell geometry", *Medical Eng. Phys.*, **31**(4), 441-447.

Carrera, E. and Giunta, G. (2010), "Refined beam theories based on a unified formulation", *Int. J. Appl. Mech.*, **2**(1), 117-143.

Carrera, E., Giunta, G., Nali, P. and Petrolo, M. (2010), "Refined beam elements with arbitrary cross-section geometries", *Comput. Struct.*, **88**(5-6), 283-293.

Carrera, E., Giunta, G. and Petrolo, M. (2011), *Beam structures: classical and advanced theories*, John Wiley & Sons.

Carrera, E. and Petrolo, M. (2012), "Refined one-dimensional formulations for laminated structure analysis", *AIAA J.*, **50**(1), 176-189.

Carrera, E., Petrolo, M. and Varello, A. (2012), "Advanced beam formulations for free vibration analysis of conventional and joined wings", *J. Aerospace Eng.*, **25**(2), 282-293.
Carrera, E. and Varello, A. (2012), "Dynamic response of thin-walled structures by variable kinematicone-dimensional models", *J. Sound Vib.*, **331**(24), 5268-5282.
Cheng, G., Loree, H., Kamm, R., Fishbein, M. and Lee, R. (1993), "Distribution of circumferential stress in ruptured and stable atherosclerotic lesions. A structural analysis with histopathological correction", *Circulation*, **87**(4), 1179-1187.
Şimşek, M. (2010), "Vibration analysis of a functionally graded beam under a moving mass by using different beam theories", *Compos. Struct.*, **92**(4), 904-917.
Davies, M. (1996), "Stability and instability: two faces of coronary atherosclerosis. The Paul Dudley White lecture 1995", *Circulation*, **94**(8), 2013-2020.
Euler, L. (1744), *De Curvis Elasticis*, *Bousquet*, Lausanne and Geneva.
Ganesan, R. and Zabihollah, A. (2007a), "Vibration analysis of tapered composite beams using a higher-order finite element, Part I: formulation", *Compos. Struct.*, **77**(3), 306-318.
Ganesan, R. and Zabihollah, A. (2007b), "Vibration analysis of tapered composite beams using ahigher-order finite element, Part II: parametric study", *Compos. Struct.*, **77**(3), 319-330.
Gao, H. and Long, Q. (2008), "Effects of varied lipid core volume and fibrous cap thickness on stress distribution in carotid arterial plaques", *J. Biomech.*, **41**(14), 3053-3059.
Gao, H., Long, Q., Graves, M., Gillard, J. and Li, Z. (2008), "Carotid arterial plaque stress analysis using fluid-structure interactive simulation based on in-vivo magnetic resonance images of four patients", *J. Biomech.*, **42**(10), 1416-1423.
Gao, H., Long, Q., Graves, M., Gillard, J. and Li, Z. (2009), "Study of reproducibility of human arterial plaque reconstruction and its effects on stress analysis based on multispectral in vivo magnetic resonance imaging", *J. Magn. Reson. Imaging*, **30**(1), 85-93.
Holzapfel, G.A., Sommer, G. and Regitnig, P. (2004), "Anisotropic mechanical properties of tissue components in human atherosclerotic plaques", *J. Biomech. Eng. - T ASME*, **126**(5), 657-665.
Huang, H., Virmani, R., Younis, H., Burke, A., Kamm, R. and Lee, R. (2001), "The impact of calcification on the biomechanical stability of atherosclerotic plaques", *J. Biomech. Eng. - T ASME*, **103**(8), 1051-1056.
Jones, R. (1999), *Mechanics of composite materials*, 2nd Ed., Taylor & Francis, Philadelphia.
Kant, T. and Gupta, A. (1988), "A finite element model for a higher-order shear deformable beam theory", *J. Sound Vib.*, **125**(2), 193-202.
Kapania, K. and Raciti, S. (1989), "Recent advances in analysis of laminated beams and plates, Part II:vibrations and wave propagation", *AIAA J.*, **27**(7), 935-946.
Kock, S., Nygaard, J., Eldrup, N., Fründ, E., Klaerke, A., Paaske, W., Falk, E. and Yong Kim, W. (2008), "Mechanical stresses in carotid plaques using MRI-based fluid-structure interaction models", *J. Biomech.*, **41**(8), 1651-1658.
Li, Z., Howarth, S., Trivedi, R., U-King-Im, J., Graves, M., Brown, A., Wang, L. and Gillard, J. (2006), "Stress analysis of carotid plaque rupture based on in vivo high resolution MRI", *J. Biomech.*, **39**(14), 2611-2622.
Li, Z., Tang, T., U-King-Im, J., Graves, M., Sutcliffe, M. and Gillard, J. (2008), "Assessment of carotid plaque vulnerability using structural and geometrical determinants", *Circulation*, **72**(7), 1092-1099.
Librescu, L. and Na, S. (1998), "Dynamic response of cantilevered thin-walled beams to blast and sonic-boom loadings", *Shock Vib.*, **5**(1), 23-33.
Loree, H., Kamm, R., Stringfellow, R. and Lee, R. (1992), "Effects of fibrous cap thickness on peakcircumferential stress in model atherosclerotic vessels", *Circulation Res.*, **71**(4), 850-858.
Marur, S.R. and Kant, T. (1996), "Free vibration analysis of fiber reinforced composite beams using higher order theories and finite element modeling", *J. Sound Vib.*, **194**(3), 337-351.
Marur, S.R. and Kant, T. (1997), "On the performance of higher order theories for transient dynamic analysis of sandwich and composite beams", *Comput. Struct.*, **65**(5), 741-759.
Marur, S.R. and Kant, T. (2007), "On the angle ply higher order beam vibrations", *Comput. Mech.*, **40**(1),

25-33.
Na, S. and Librescu, L. (2001), "Dynamic response of elastically tailored adaptive cantilevers of nonuniformcross section exposed to blast pressure pulses", *Int. J. Impact Eng.*, **25**(9), 847-867.
Petersen, S., Peto, V., Rayner, M., Leal, J., Luengo-Fernandez, R. and Gray, A. (2005), *European Cardiovascular Disease Statistics*, British Heart Foundation (BHF), London.
RamalingerswaraRao, S. and Ganesan, N. (1995), "Dynamic response of tapered composite beams usinghigher order shear deformation theory", *J. Sound Vib.*, **187**(5), 737-756.
Rodríguez, J., Ruiz, C., Doblaré, M. and Holzapfel, G. (2008), "Mechanical stresses in abdominal aorticaneurysms: influence of diameter asymmetry and material anisotropy", *J. Biomech. Eng. - T ASME*, **130**(2), 021023(1-10).
Silvestre, N. and Camotim, D. (2002), "Second-order generalised beam theory for arbitrary orthotropic materials", *Thin Wall. Struct.*, **40**(9), 791-820.
Tang, D., Yang, C., Mondal, S., Liu, F., Canton, G., Hatsukami, T. and Yuan, C. (2008), "A negative correlation between human carotid atherosclerotic plaque progression and plaque wall stress: in vivo MRI-based 2D/3D FSI models", *J. Biomech.*, **41**(4), 727-736.
Timoshenko, S. (1921), "On the correction for shear of the differential equation for transverse vibrations of prismatic bars", *Philos. Mag.*, **41**, 744-746.
Tong, X., Tabarrok, B. and Yeh, K.Y. (1995), "Vibration analysis of Timoshenko beams with nonhomogeneity and varying cross-section", *J. Sound Vib.*, **186**(5), 821-835.
Varello, A. and Carrera, E., "Static and dynamic analysis of a thin-walled layered cylinder by refined 1DTheories", *Proceedings of the 10th World Congress on Computational Mechanics*, São Paulo, Brazil, July.
Yu, W., Volovoi, V., Hodges, D. and Hong, X. (2002), "Validation of the variational asymptotic beam sectional analysis (VABS)", *AIAA J.*, **40**(10), 2105-2113.
Yuan, C., Kerwin, W., Ferguson, M., Polissar, N., Zhang, S., Cai, J. and Hatsukami, T. (2002), "Contrast-enhanced high resolution MRI for atherosclerotic carotid artery tissue characterization", *J. Mag. Reson. Imaging*, **15**(1), 62-67.

FC